

NASA/TM-2003-212402  
ARL-TR-2959



# Modeling the Interactions Between Multiple Crack Closure Mechanisms at Threshold

*John A. Newman*  
*U.S. Army Research Laboratory*  
*Vehicle Technology Directorate*  
*Langley Research Center, Hampton, Virginia*

*William T. Riddell*  
*U.S. Department of Transportation*  
*Volpe National Transportation Systems Center*  
*Cambridge, Massachusetts*

*Robert S. Piascik*  
*Langley Research Center, Hampton, Virginia*

National Aeronautics and  
Space Administration

Langley Research Center  
Hampton, Virginia 23681-2199

---

May 2003

## Abstract

*A fatigue crack closure model is developed that includes interactions between the three closure mechanisms most likely to occur at threshold; plasticity, roughness, and oxide. This model, herein referred to as the CROP model (for Closure, Roughness, Oxide, and Plasticity), also includes the effects of out-of-plane cracking and multi-axial loading. These features make the CROP closure model uniquely suited for, but not limited to, threshold applications. Rough cracks are idealized here as two-dimensional sawtooths, whose geometry induces mixed-mode crack-tip stresses. Continuum mechanics and crack-tip dislocation concepts are combined to relate crack face displacements to crack-tip loads. Geometric criteria are used to determine closure loads from crack-face displacements. Finite element results, used to verify model predictions, provide critical information about the locations where crack closure occurs.*

## Introduction

Fatigue crack closure occurs when crack faces contact during cyclic loading. It is widely assumed that closed cracks are shielded from fatigue loads and no fatigue damage occurs while crack faces are in contact (ref. 1). Further, fatigue cracks are normally closed during a portion of the load cycle, so the applied  $\Delta K$  is not a true crack-tip driving force. Instead fatigue crack growth (FCG) rate,  $da/dN$ , is related to an effective  $\Delta K$  defined in Equations 1 and 2, where  $K_{cl}$  is the stress intensity below which the crack is closed. Closure can even occur under tensile loading and has been used to explain load ratio effects on FCG (ref. 1).

$$\Delta K_{eff} = K_{max} - K_{cl} \quad (1)$$

$$da/dN = f(\Delta K_{eff}) \quad (2)$$

## Crack Closure Mechanisms

Elber, the first to propose fatigue crack closure, suggested that crack face contact was due to residual plastic deformation in the wake of a propagating crack (ref. 1). This mechanism was coined plasticity-induced crack closure (PICC) as other closure mechanisms were suggested. Adams (ref. 2), Purshothaman and Tien (ref. 3), and Walker and Beevers (ref. 4) suggested contact of misaligned rough crack surfaces (roughness-induced crack closure, RICC) as a closure mechanism. The formation of a voluminous oxide layer along the crack faces (oxide-induced crack closure, OICC) was suggested as a closure mechanism by Walker and Beevers (ref. 4), Endo, *et al.* (ref. 5), and Suresh, *et al.* (ref. 6). For Paris regime FCG of most engineering alloys, PICC is the dominant closure mechanism (*i.e.* RICC and OICC are second-order effects) and PICC models successfully predict closure loads and FCG rates (ref. 7). Normally, RICC and OICC only become first-order effects as crack-face asperities and oxide layers become large relative to crack-tip displacements near the FCG threshold (ref. 8).<sup>\*</sup> PICC is always a first-order effect and accounts for as much as 80% of the closure effects at threshold (ref. 9). Although

---

<sup>\*</sup> In cases of extreme crack path tortuosity (ref. 10) and aggressive environment (ref. 5) RICC and OICC can be significant even in the Paris regime.

typically studied individually, it is likely that all three mechanisms (PICC, RICC, and OICC) are operative and interacting, especially near the FCG threshold. To accurately model closure at threshold, the combined influences of PICC, RICC, and OICC must be considered.

## Crack Closure Models

Many models have been developed to predict fatigue crack closure behavior. However, most models are limited to a single closure mechanism and are unable to describe the interactions between multiple closure mechanisms likely to occur near the FCG threshold. Plasticity-based models adequately predict R-effects in the Paris regime where PICC dominates, but lack fidelity at threshold because RICC and OICC are neglected (ref. 9). RICC and OICC models have been developed to predict closure loads at threshold, but are limited because PICC is not considered, or they rely on empirical relations (which may be application specific) (refs. 11 and 12). Suresh and Ritchie were among the first to model rough cracks as a two-dimensional sawtooth wave (ref. 11). This rough crack geometry produces mixed-mode crack-tip stresses, and both opening and sliding mode crack-face displacements. As modeled by Suresh and Ritchie, mode II displacements do not return to zero upon unloading, creating misalignment between mating crack surfaces. Wang, *et al.* (ref. 12) developed a similar model, where mode II displacements were calculated in terms of dislocations emitted from a single slip plane coinciding with the crack-tip direction. Because the Wang model only allows slip to occur along a single plane, only sliding mode displacements occur, although mixed-mode crack-tip stresses are expected. However, neither model considers crack-wake plasticity or oxides.

Llorca (ref. 13), Garcia and Seheitoglu (refs. 14 and 15), Chen and Lawrence (ref. 16), and Ravichandran (refs. 17 and 18) have proposed more complicated RICC models (in terms of computation requirements). Llorca developed a finite difference model, which also idealized the crack profile as a sawtooth wave. The most important variables influencing closure levels for this model were crack tilt angle and average direction of crack growth (considering out-of-plane cracking). Furthermore, RICC was discontinuous; for instance, closure was greatest as the crack was changing direction. This observation is significant because it suggests closure is more likely to occur at specific crack-wake features (*i.e.*, at sawtooth peaks and valleys). Garcia and Seheitoglu modeled rough crack asperities as three-dimensional features randomly distributed along the crack surface. Statistical means were used to evaluate asperity heights and radii. The crack surface was divided into multiple strips, and each strip was treated as a rough surface contact problem. Chen and Lawrence investigated the combined effects of RICC and PICC by altering a strip yield model, developed by Newman (ref. 19), for a sawtooth crack. The Chen and Lawrence model is among the first to describe the interaction of closure mechanisms (RICC and PICC). The Ravichandran model also used a sawtooth profile and predicted closure levels as a function of microstructural scale (*i.e.*, grain size), dislocation density, and yield stress. As with the Wang model, sliding mode displacements were a result of crack-tip dislocation emission in the Ravichandran model.

Newly developed numerical models (refs. 13-18) are more complex and sophisticated than the analytical models of Suresh and Ritchie (ref. 11) and Wang, *et al.* (ref. 12); some are able to consider multiple closure mechanisms. Despite the added complexity, no model adequately predicts the combined effects of PICC, RICC, and OICC, both near the FCG threshold and in the Paris regime. Ideally, a closure model would be complex enough to consider the combined effects of PICC, RICC, and OICC (the closure mechanisms considered most likely at threshold), yet be computationally simple and analytical in nature.

## Objectives

The objective of this paper is to develop an analytical fatigue crack closure model that predicts and describes contributions and interactions of PICC, RICC, and OICC; considered the most likely closure mechanisms at threshold. The closure model developed in this paper will be called the CROP model for Closure, Roughness, Oxide, and Plasticity. Special considerations will be made for near-threshold FCG scenarios, but this model will not be limited to low  $\Delta K$ . The crack geometry is idealized as a sawtooth wave, but modified to allow out-of-plane cracking. To develop this model, it is necessary to characterize crack-face displacements of rough cracks, and include crack-wake plasticity and oxide. Cracks might kink on a macroscale due to mixed-mode loading or geometry (ref. 20). However, it is the development of kinks on a microscale (*i.e.* roughness), due to microstructural features (ref. 21), that are of primary interest in this paper. Most existing closure models include a single closure mechanism and work well for either Paris or threshold FCG, but not both. By including multiple closure mechanisms, it is hoped that the CROP model will work for a broad range of FCG scenarios. Finally, if supported by experimental data (see ref. 22), the CROP model can be used to study interactions between PICC, RICC, and OICC.

## Model Development

Step-by-step development of the CROP closure model is presented in this section. In addition to modeling PICC, RICC, and OICC, out-of-plane cracking and a limited amount of (applied) mixed-mode loading are considered.<sup>†</sup> Inclusion of each mechanism is discussed separately. Crack-face displacements are characterized and compared with crack-wake effects (*i.e.*, plasticity, roughness, and oxide) to compute closure loads.

### Consideration of RICC and out-of-plane cracking

Rough crack surfaces are modeled here as a sawtooth wave (*i.e.*, a series of two-dimensional, rigid, triangular asperities, of equal size and shape) similar to the geometry of existing closure models (refs. 11-13, 16, 17). A schematic of this sawtooth crack profile, modified to consider out-of-plane cracking (a macroscopic deviation from global coordinates by an angle,  $\gamma$ ), is shown in Figure 1.<sup>‡</sup> Characteristic roughness parameters (asperity length,  $g$ , and asperity angle,  $\alpha$ ) should be obtained from real crack surfaces, or related to microstructural features, such as grain size. The sawtooth geometry is a reasonable approximation for most rough crack surfaces, and simplifies the geometric conditions of crack face contact. Three coordinate systems are required to describe the crack geometry in Figure 1. First, a global coordinate frame is used to describe loading or specimen geometry, and from which out-of-plane crack deflection is measured. The global coordinate frame is labeled by  $X$  and  $Y$  in the figure. Next, a local coordinate frame is needed. The  $x$ -axis of the local coordinate frame coincides with the nominal crack direction (average direction of FCG from a macroscopic point of view). This coordinate frame is labeled in Figure 1 by  $x$  and  $y$ . Finally, a crack-tip coordinate frame is needed, whose  $x$ -axis coincides with the orientation of the crack-tip on a microscale. As shown in Figure 1, the crack-tip coordinate frame is labeled by  $x'$  and  $y'$ . When considering closure of rough cracks, it is convenient to describe crack face displacements using both local and crack-tip coordinates.

---

<sup>†</sup> The CROP model is limited to cases where mode I loading is dominant. Problems arise when sliding-mode crack closure (SMCC) occurs, a result of mode II loading, as described in detail elsewhere (ref. 23).

<sup>‡</sup> ASTM standards permit neglecting out-of-plane cracking at angles less than  $10^\circ$ , and FCG data for angles up to  $20^\circ$  is considered valid, but out-of-plane cracking must be reported (ref. 24).

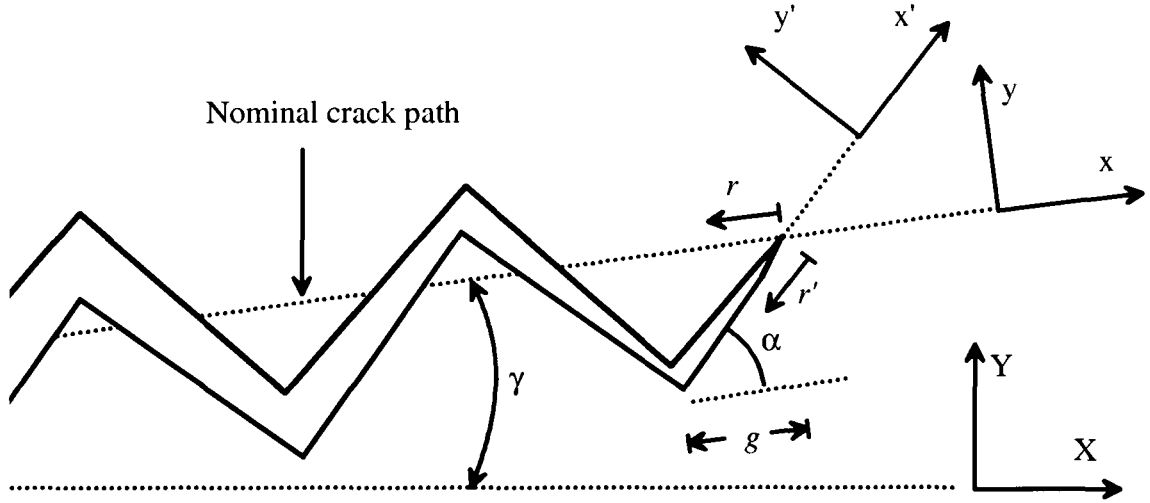


Figure 1. A schematic of the idealized crack configuration used by the CROP model; a two-dimensional sawtooth subject to out-of-plane cracking.

### Stress intensity factors

Crack-tip stress-intensity factors for out-of-plane rough cracks are approximated using analytical stress solutions for two crack configurations. Solutions of angled straight cracks and angled, infinitesimal kinks at the tip of an otherwise straight cracks are used to predict the effects of out-of-plane cracking and crack roughness, respectively. The methodology used to determine crack-tip stresses for rough out-of-plane cracks is shown schematically in Figure 2. First, the analytical solution for an angled straight crack is used to predict the effects of out-of-plane cracking. This crack configuration is shown in Figure 2a under general planar loading, *i.e.*, with non-zero  $\sigma_Y$ ,  $\sigma_X$ , and  $\tau_{XY}$ . Crack-tip stress-intensity factors are obtained for this configuration by transforming the applied loads (global coordinates) into local coordinates. These transformed stresses are then used to calculate the stress-intensity factors shown in Equations 3 and 4, where  $K_{Ig} = \sigma_Y \sqrt{\pi a}$ ,  $K_{IIg} = \tau_{XY} \sqrt{\pi a}$ , and  $K_{Og} = \sigma_X \sqrt{\pi a}$ . The stress intensity factor  $K_{Og}$  accounts for non-singular stresses parallel to cracks that contribute to the singularity upon meandering (refs. 25 and 26). Note that  $2a$  is defined as the crack length projected onto the plane perpendicular to  $\sigma_Y$ ; and is used because this is the dimension normally measured during fatigue crack growth (FCG) tests. The actual crack length is  $2a/\cos(\gamma)$ .

$$K_{I\text{Local}} = K_{Ig} \sqrt{\cos^3(\gamma)} - 2 K_{IIg} \sin(\gamma) \sqrt{\cos(\gamma)} + K_{Og} \left[ \frac{\sin^2(\gamma)}{\sqrt{\cos(\gamma)}} \right] \quad (3)$$

$$K_{II\text{Local}} = K_{Ig} \sin(\gamma) \sqrt{\cos(\gamma)} - K_{IIg} \left[ \frac{\cos^2(\gamma)}{\sqrt{\cos(\gamma)}} \right] - K_{Og} \sin(\gamma) \sqrt{\cos(\gamma)} \quad (4)$$

The stress intensity factors for a straight crack with an infinitesimal kink are used to approximate stress-intensity factors for rough (sawtooth) cracks (see Figure 2b) (ref. 27). These relations are given as Equations 5 and 6, but are valid only if the kink length,  $\delta a$ , is small compared to the K-dominated region at the crack-tip (ref. 28). It will be shown later that Equations 5 and 6 are also valid for sawtooth cracks. Note that local stress intensity factors of Equations 3 and 4 are used in Equations 5 and 6 allowing

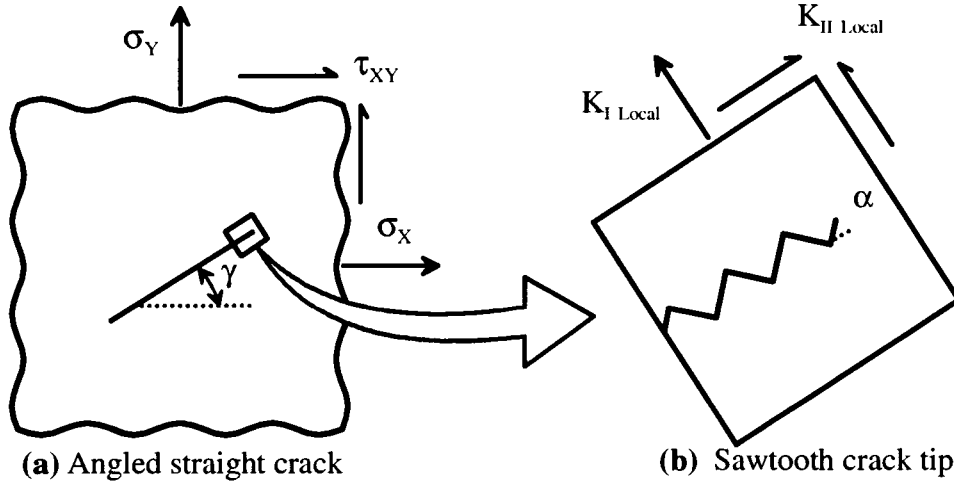


Figure 2. Schematics to describe analytical stress-intensity factor solutions for two crack configurations – an angled straight crack and a straight crack with a kinked crack tip.

simultaneous consideration of crack roughness and out-of-plane cracking. As schematically shown in Figure 2, the angled straight crack solutions are used first to determine the macroscopic effects of out-of-plane cracking (Equations 3 and 4), then, the microscopic crack roughness effects are evaluated (Equations 5 and 6). The stress intensity factors are expressed in terms of globally applied stress-intensity factors because these quantities are normally used to describe FCG tests.

$$K_I = \cos^2\left(\frac{\alpha}{2}\right) \left[ K_{I \text{ Local}} \cos\left(\frac{\alpha}{2}\right) - 3 K_{II \text{ Local}} \sin\left(\frac{\alpha}{2}\right) \right] \quad (5)$$

$$K_{II} = \cos\left(\frac{\alpha}{2}\right) \left[ K_{I \text{ Local}} \sin\left(\frac{\alpha}{2}\right) \cos\left(\frac{\alpha}{2}\right) + K_{II \text{ Local}} \left[ 1 - 3 \sin^2\left(\frac{\alpha}{2}\right) \right] \right] \quad (6)$$

### Elastic crack face displacements

Elastic crack-face displacements are functions of the crack-tip stress-intensity factors determined in the previous section. Because all rough cracks are subjected to a mixed-mode stress state, both opening and sliding mode crack-face displacements (mode I and mode II, respectively) are expected. Sliding mode displacements create misalignment of crack-face asperities, *i.e.*, RICC. Elastic crack face displacements for straight cracks under plane-strain conditions and mixed-mode planar loading are shown in Equation 7, where  $E$  is the elastic modulus,  $\nu$  is Poisson's ratio, and  $r'$  is the distance behind the crack tip (see Figure 1) (ref. 26). Note that  $r' = r / \cos(\alpha)$  and the total relative displacements between the two crack faces are  $2u'$  and  $2v'$ . Primed quantities indicate use of crack-tip coordinates and  $r$  is defined with respect to the local coordinate frame. Plane-strain conditions were adopted because the CROP model is intended for threshold applications; for typical FCG specimens near threshold, most of the crack front is under plane-strain conditions. It will be shown later that Equation 7 is valid in the crack-tip vicinity for sawtooth cracks. The crack-face displacements of Equation 7 are expressed in crack-tip coordinates, but can be transformed to local coordinates using Equation 8. Local coordinates will be convenient when considering crack closure.

$$\begin{Bmatrix} u' \\ v' \end{Bmatrix} = \left[ \frac{4(1-\nu^2)}{E} \sqrt{r'/2\pi} \right] \begin{Bmatrix} K_{II} \\ K_I \end{Bmatrix} \quad (7)$$

$$\begin{Bmatrix} u \\ v \end{Bmatrix} = \begin{bmatrix} \cos(\alpha) & -\sin(\alpha) \\ \sin(\alpha) & \cos(\alpha) \end{bmatrix} \begin{Bmatrix} u' \\ v' \end{Bmatrix} \quad (8)$$

## Consideration of crack-tip plasticity and PICC

As a cracked body is loaded, a plastic zone forms at the crack-tip (refs. 29 and 30). Crack-tip plasticity for mixed-mode loading will produce a crack-tip opening displacement (CTOD) and a crack-tip sliding displacement (CTSD).<sup>§</sup> Existing crack-tip slip models for mode I straight cracks (refs. 31 and 32) consider all crack-tip deformations as the result of dislocation motion along planes that coincide with the maximum singular shear stress. Although these models were developed for mode I loading, this approach is generalized by determining the orientation of extreme values of the singular crack-tip shear stresses for mixed-mode loading are modified to estimate plastic displacements of a mixed-mode crack tip. On a microscale, plasticity is the result of dislocation glide originating near the crack tip (ref. 33). Near the crack-tip, dislocation pairs of opposite sign are created. Dislocations of one sign are attracted to the crack tip, where they are annihilated, producing plastic displacements. Dislocations of the opposite sign are driven away from the crack-tip. Ultimately, these dislocations will either (1) stop at a barrier, such as a particle interface or grain boundary (refs. 34-36), or (2) go far from the crack-tip where a reduction in dislocation driving force (stress) occurs (refs. 33 and 37). For the model developed herein, slip is assumed to occur by edge dislocations that glide freely along slip paths until reaching the edge of the plastic zone, which acts as a Peierls-Nabarro energy barrier; here stresses become too small for further dislocation movement. As in previous crack-tip dislocation emission models, dislocations are assumed to travel along planes originating at the crack-tip.<sup>\*\*</sup> The plane-strain plastic zone radius is defined in Equation 9, as a function of angle from the crack plane,  $\theta$  (ref. 39). Equation 9 is based on linear-elastic material behavior and assumes no stress redistribution due to crack-tip plasticity; this radius is that of the elastic solution whose vonMises equivalent stress corresponds to yielding. The increase in plastic zone due to stress redistribution was accounted for by increasing the plastic zone of Equation 9 by a factor of 1.828 (see Equation 10). This constant was chosen such that the CTOD (which will be calculated using Equation 9) for a straight crack matched the theoretical value ( $K^2 / E \sigma_0$ ). This relation is used to determine the monotonic plastic zone (MPZ) associated with  $K_{max}$ .<sup>††</sup>

It is recognized that slip occurs along preferred slip planes that depend on microstructure and local shear stress (acting on these planes). However, it is assumed that slip planes (on average) coincide with planes of extrema in elastic crack-tip shear stress,  $\tau_{\theta}$ . This combination of dislocation emission and continuum mechanics is appropriate when crack-tip deformation occurs in multiple grains along the crack front. The elastic, singular crack-tip stresses for mixed-mode loading under plane-strain conditions are given in Equation 11 (ref. 26). The directions of shear extrema,  $\theta_i$ , satisfy Equation 12 (which is obtained

<sup>§</sup> In general, CTOD and CTSD may include both elastic and plastic components. However, Equation 7 indicates no elastic displacement exists at the crack tip. For this model CTOD and CTSD describe only plastic crack-tip displacements.

<sup>\*\*</sup> Slip is described as occurring on planes whose projection into the two-dimensional model is a line. However, the phrase "slip plane" is used to be consistent with existing literature (ref. 38).

<sup>††</sup> The MPZ is the crack-tip region where plasticity occurs during loading, and is associated with  $K_{max}$ . The cyclic plastic zone (CPZ), a subset of the MPZ where reverse plasticity occurs during unloading, is associated with  $\Delta K$ . The CPZ will be discussed later.

$$r_p^* = \frac{1}{2\pi\sigma_o^2} \left[ \begin{aligned} & K_{I,Local}^2 \left\{ \cos^2\left(\frac{\theta}{2}\right) \left[ 3\sin^2\left(\frac{\theta}{2}\right) + (1-2\nu)^2 \right] \right\} \\ & + K_{II,Local}^2 \left\{ 3 + \sin^2\left(\frac{\theta}{2}\right) \left[ (1-2\nu)^2 - 9\cos^2\left(\frac{\theta}{2}\right) \right] \right\} \\ & + K_{I,Local} K_{II,Local} \sin(\theta) \left[ 3\cos(\theta) - (1-2\nu)^2 \right] \end{aligned} \right] \quad (9)$$

$$r_p = 1.828 r_p^* \quad (10)$$

by setting the derivative of  $\tau_{r\theta}$ , with respect to  $\theta$  to zero). This equation is transcendental and must be solved numerically, *i.e.* no closed form solution exists for  $\theta_i$ . Equation 12 has three solutions except for straight cracks under pure mode I loading, which have only two solutions. A plot of the singular shear stress coefficient ( $\tau_{r\theta}$  multiplied by  $\sqrt{2\pi r}$ ) versus angle from the crack-tip direction is shown in Figure 3a for a crack configuration described by  $\alpha = 45^\circ$ ,  $\gamma = 10^\circ$ ,  $K_{Ie} = 1$ , and  $K_{IIe} = 0$ . The three local extrema are indicated by vertical dotted lines and labeled in Figure 3a. A schematic of the corresponding plastic zone (calculated by Equation 10) is shown in Figure 3b. The slip planes indicated in Figure 3a are shown in Figure 3b as solid lines emanating from the crack tip. Although the extrema of crack-tip shear do not exactly coincide with extrema in plastic zone radius, the two differ by less than  $30^\circ$ .

$$\begin{Bmatrix} \sigma_r \\ \sigma_{\theta\theta} \\ \tau_{r\theta} \end{Bmatrix} = \frac{K_I}{\sqrt{2\pi r}} \cos\left(\frac{\theta}{2}\right) \begin{Bmatrix} 1 + \sin\left(\frac{\theta}{2}\right) \\ \cos^2\left(\frac{\theta}{2}\right) \\ \sin\left(\frac{\theta}{2}\right) \cos\left(\frac{\theta}{2}\right) \end{Bmatrix} + \frac{K_{II}}{\sqrt{2\pi r}} \begin{Bmatrix} \sin\left(\frac{\theta}{2}\right) \left[ 1 - 3\sin^2\left(\frac{\theta}{2}\right) \right] \\ -3\sin\left(\frac{\theta}{2}\right) \cos^2\left(\frac{\theta}{2}\right) \\ \cos\left(\frac{\theta}{2}\right) \left[ 1 - 3\sin^2\left(\frac{\theta}{2}\right) \right] \end{Bmatrix} \quad (11)$$

$$K_I \left[ 1 - 3\sin^2\left(\frac{\theta_i}{2}\right) \right] = K_{II} \tan\left(\frac{\theta_i}{2}\right) \left[ 7 - 9\sin^2\left(\frac{\theta_i}{2}\right) \right] \quad (12)$$

The dislocation distribution along individual slip planes has been solved assuming a constant shear stress in the plastic zone (*e.g.*, assuming elastic-perfectly plastic behavior at the crack-tip, use  $\tau = 0.5 \sigma_o$ ) and no interaction between slip planes. The total slip along a slip plane of length  $r_p$  is given by Equation 13, where  $E$  is the elastic modulus,  $\nu$  is Poisson's ratio,  $n$  is the total number of edge dislocations, and  $b$  is the magnitude of the Burger's vector (ref. 40).

$$B = nb = \frac{r_p \sigma_o \pi (1 - \nu^2)}{E} \quad (13)$$

Using this relation, plastic crack-tip deformations (CTOD' and CTSD') are computed by summing the vector components of each slip plane (in crack-tip coordinates) as shown in Equations 14 and 15. (Again, primed quantities correspond to crack-tip coordinates.) The symbol  $\Sigma$  indicates summation over the range



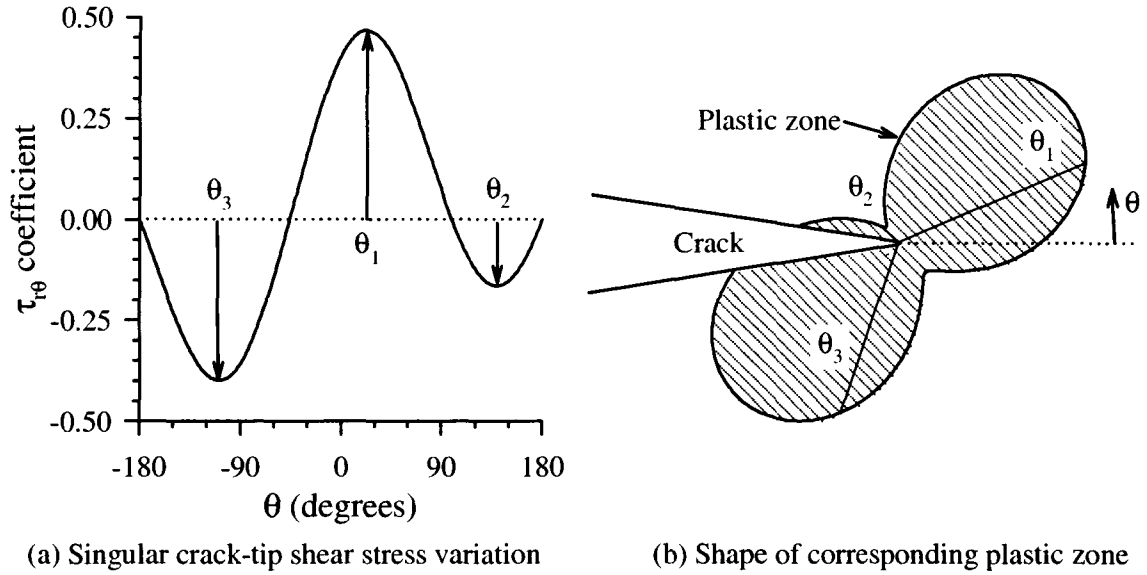


Figure 3. The effect of mixed-mode loads on crack-tip stresses and the crack-tip plastic zone.

of the index 'i', which typically ranges from one to three (the total number of slip planes).<sup>††</sup> Conversion to local coordinates involves the same transformation given in Equation 8.

$$CTOD' = \sum B_i \sin(\theta_i) \quad (14)$$

$$CTSD' = \sum B_i \cos(\theta_i) \quad (15)$$

The cyclic plastic zone (CPZ) is a subset of the MPZ, where reverse plasticity occurs during unloading. The size of the CPZ is proportional to  $\Delta K^2$ , and the shape can be calculated using Equations 9 and 10, by inserting one-half of the cyclic stress intensity factors in place of the maximum values (*e.g.*,  $K_{I \text{ Local}}$  is replaced by  $\frac{1}{2} \Delta K_{I \text{ Local}}$ ). Reversed plasticity in the CPZ leads to a reduction in residual CTOD and CTSD. For modeling purposes, reversed slip is assumed to occur along the same slip planes as for loading, but using the CPZ boundary as maximum slip length and replacing  $\tau$  in Equation 13 with  $-\tau$ . Because the MPZ and CPZ radii are proportional to  $(K_{\max})^2$  and  $\frac{1}{2}(\Delta K)^2$ , respectively, CTOD and CTSD are also a function of  $K_{\max}$  and  $\Delta K$ , as in Equation 16. The subscript 'max' corresponds to maximum values of that quantity, which occur at maximum load.<sup>§§</sup>

$$\begin{Bmatrix} CTOD \\ CTSD \end{Bmatrix} = \left[ 1 - \left( \frac{\Delta K}{2 K_{\max}} \right)^2 \right] \begin{Bmatrix} CTOD_{\max} \\ CTSD_{\max} \end{Bmatrix} \quad (16)$$

Although RICC and OICC are most significant at FCG threshold, PICC is still a major contributor and must be considered (refs. 9 and 41). Thus, a complete discussion of crack plasticity must include crack-wake deformation. A PICC model by Budiansky and Hutchinson (ref. 42) relates crack-wake plasticity to

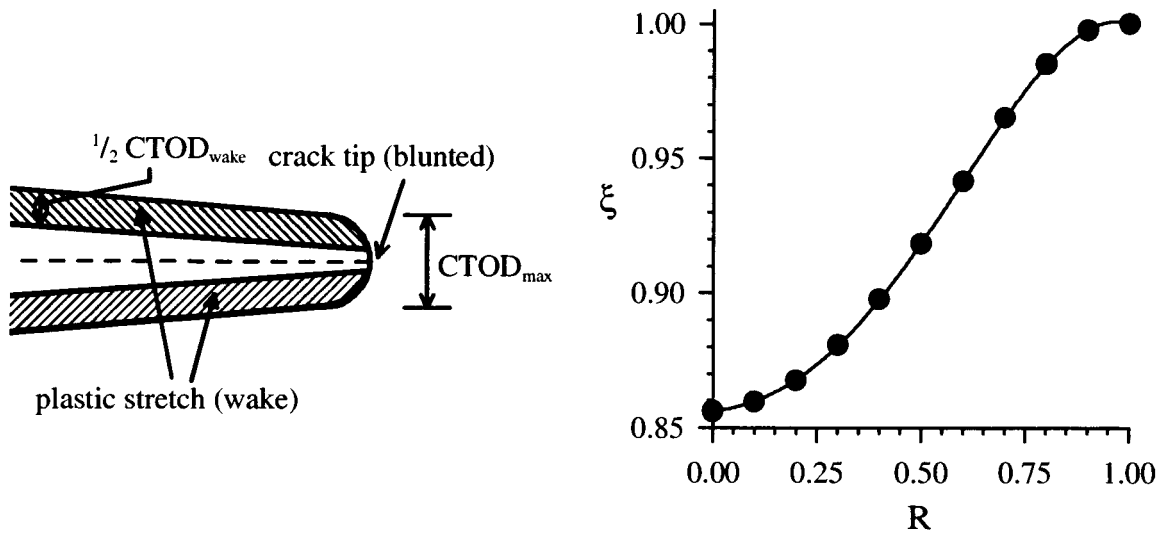
<sup>††</sup> Only two slip planes exist for a straight crack (*i.e.*,  $\alpha = 0$ ), so 'i' ranges from 1 to 2 in this case.

<sup>§§</sup> This is only true in cases of proportional loading – that is, the ratio  $K_{II}/K_I$  remains constant during the load cycle – which is an assumption of the CROP model.

the CTOD. A value less than  $CTOD_{max}$  (the CTOD at maximum load) is used to account for reversed crack-tip plasticity during unloading. For  $R = 0$ , Budiansky and Hutchinson calculate the residual plastic wake as approximately 86% of  $CTOD_{max}$ , or  $\xi = 0.86$ . The normalized crack-wake plasticity,  $\xi$  is defined in Equation 17, where  $CTOD_{wake}$  is the total residual plastic wake (half associated with each crack face). The relation between  $CTOD_{max}$  and  $CTOD_{wake}$  is shown schematically in Figure 4a. Here, a straight crack is shown under load with a blunted crack tip. Residual crack-wake plasticity is indicated as shaded regions along each crack face. Although plastic deformation partially fills the crack mouth in this schematic, the crack is shown open. Using results from Budiansky and Hutchinson (open circular symbols), a plot of  $\xi$  versus applied  $R$  is shown in Figure 4b along with a least squares fitted (4<sup>th</sup> order) polynomial. This fitted polynomial is expressed symbolically in Equation 18, and is used to estimate  $\xi$  as a function of  $R$ . Using Equation 18 instead of the entire procedure developed by Budiansky and Hutchinson simplifies evaluation of the CROP closure model.

$$\xi = \frac{CTOD_{wake}}{CTOD_{max}} \quad (17)$$

$$\xi = 0.8561 + 0.0205 \cdot R + 0.1438 \cdot R^2 + 0.2802 \cdot R^3 - 0.3007 \cdot R^4 \quad (18)$$



(a) Crack tip at maximum load

(b) Variation of  $\xi$  with  $R$  (ref. 42)

Figure 4. The relation between crack-wake and crack-tip plasticity.

## Consideration of OICC

A crack mouth oxide layer is modeled as an incompressible wedge of uniform thickness ( $t$ ) along both crack surfaces, similar to a model developed by Suresh (ref. 6). The voluminous oxide layer partially fills the crack mouth and increases closure levels. An oxide layer of finite thickness will produce higher closure levels than at higher values of  $K_{max}$  because the available crack opening is small at low values of  $K_{max}$ . Consequently, OICC is thought to be most significant near the FCG threshold (ref. 43). Naturally forming oxide layers on fresh aluminum surfaces have been measured as 10 Å thick in dry air (ref. 44), and between 50 Å and 150 Å in humid air (ref. 45), although considerable variation with environment and temperature was noted. Fretting contact of rough crack surfaces (*i.e.*, RICC) can create a large amount of

oxide debris, a result of repeated removal and regeneration of crack-mouth oxide (ref. 43). Large amounts of oxide debris may also form in aggressive (oxide producing) environments (ref. 5), where the effective oxide thickness can be much larger: up to 1000 Å in moist air for aluminum alloys (ref. 43) and 3-5 µm for steels (ref. 46). Although this model assumes a uniform oxide layer on the crack faces, modification can be made to simulate oxide debris (non-uniform). For example, oxide debris generated by fretting asperities may accumulate behind the crack tip. Oxide debris normally is thicker than an undisturbed oxide layer, expected at the crack tip. In this case, closure can be determined separately, at the location of the oxide debris and at the crack tip, using different values of oxide thickness. The crack face location with the largest closure load will contact first and dominate crack-tip behavior.

## Numerical Verification of Analytical Relations

Finite-element analyses were performed to validate crack-tip stress-intensity factor and displacement solutions (Equations 3-8) for sawtooth cracks (Figure 1) using FRANC2D (ref. 47). The asperity length,  $g$ , and asperity angle,  $\alpha$ , were varied for the sawtooth configuration. Only mode I loading was considered ( $K_{IIg} = 0$ ) with no crack meandering ( $\gamma = 0$ ) because this is the most common configuration for laboratory testing. Stress-intensity factors were extracted from the elastic solutions using the J-integral technique (ref. 48). A typical deformed (grossly exaggerated) mesh used for these analyses is shown in Figure 5 for  $\alpha = 45^\circ$  and  $g/a = 0.05$ . Taking advantage of symmetry, only half of the specimen is analyzed (using appropriate boundary conditions); the entire finite-element mesh is shown in Figure 5a. A rosette of singular quarter-point elements is used around the crack tip. The rest of the specimen is meshed with three- or four-sided quadratic elements. As seen in Figure 5b, the mesh is refined near the crack tip. At least four elements were used between the crack tip and the asperity nearest the crack tip, regardless of the asperity length,  $g$ . Further refinement of the crack-tip region changed the results by less than 2%. The sawtooth wave was extended to form at least 10 complete asperities behind the crack tip, or to the

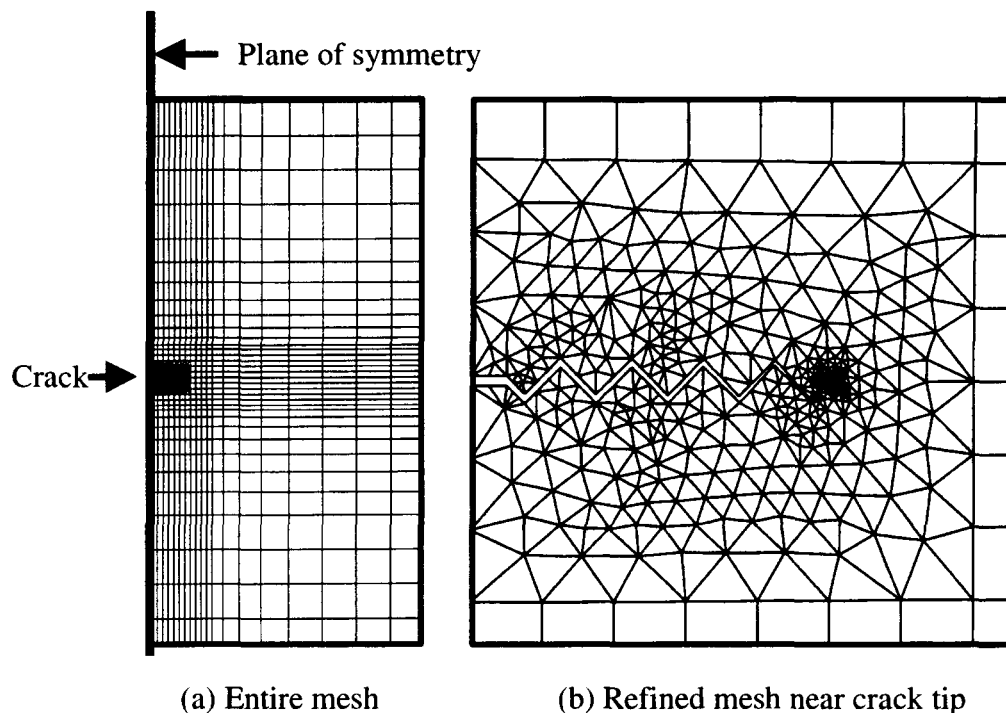


Figure 5. A typical (deformed) finite-element mesh is shown for  $\alpha = 45^\circ$  and  $g/a = 0.05$ .

specimen centerline. For convenience, the remaining crack profile was modeled as a straight line; further extension of asperities along the crack surface changed results near the crack tip ( $0 < r/g < 1$ ) by less than 1%.

Stress-intensity factors obtained from finite-element analyses are plotted in Figure 6 for asperity angles ( $\alpha$ ) ranging from  $0^\circ$  to  $45^\circ$ , and for normalized asperity length ( $g/a$ ) ranging from 0.2 to 0.002. Mode I ( $K_I$ ) results are shown in Figure 6a, and mode II ( $K_{II}$ ) results are plotted in Figure 6b. Finite-element results are shown as open symbols, while analytical solutions of Equations 5 and 6 ( $g/a = 0$ ) are shown as closed symbols. Refer to the legend in the upper left corner of the figure for symbols corresponding to specific values of  $\alpha$ . This crack configuration is shown schematically in the upper right corner of the figure. As the normalized asperity length ( $g/a$ ) approaches zero, the finite-element sawtooth crack results converge to the analytical kinked-crack solutions. This result validates the use of Equations 5 and 6 for  $g/a < 0.05$ . Similar agreement between finite-element and analytical solutions were obtained for mode II loading, but results are not presented here (ref. 23).

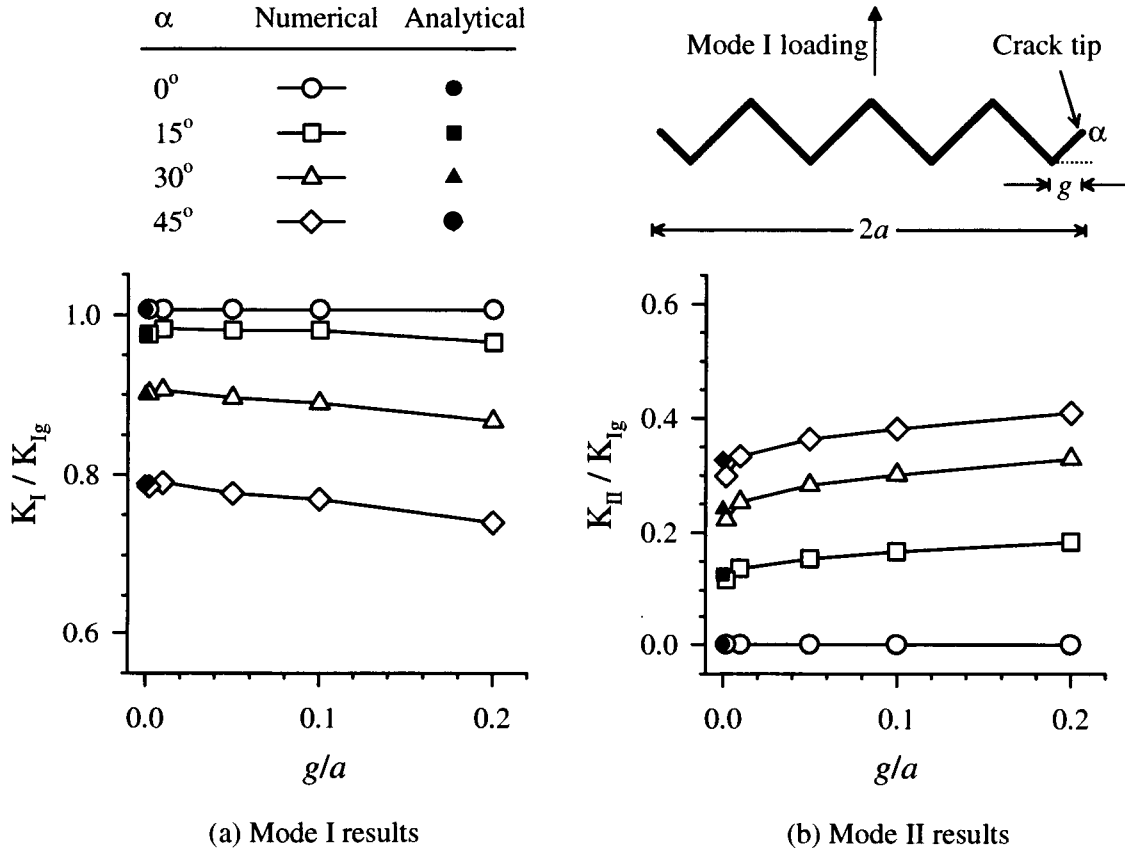


Figure 6. Stress-intensity factors for sawtooth cracks (under mode I applied loading) for  $\alpha = 0^\circ, 15^\circ, 30^\circ$ , and  $45^\circ$ .

Numerical elastic crack-face displacements are plotted against  $r/g$  (normalized distance behind the crack tip) in Figure 7 for asperity angles of  $30^\circ$  and  $45^\circ$ . Note that all quantities are presented in dimensionless form where appropriate. Dimensionless values for crack-face displacements ( $u^*$  and  $v^*$ ) are defined as follows.

$$u^* = \frac{u E}{K_{I_g} (1 - \nu^2) \sqrt{g}} \quad (19)$$

$$v^* = \frac{\nu E}{K_{I_g} (1 - \nu^2) \sqrt{g}} \quad (20)$$

Finite-element results for two values of  $g/a$  (0.1 and 0.01) are shown as open symbols (circular and square, respectively). Dashed and solid lines correspond to analytical elastic solutions of sliding and opening mode displacements predicted by Equation 7 (transformed to local coordinates), respectively. The dotted line is the (mode I) displacement solution for a straight crack (*i.e.*,  $\alpha = 0$ ) under the same mode I loading. As seen in Figure 7, mode II displacements ( $u^*$ ) match the analytical solution well, but only between the crack tip and the first asperity behind the crack tip ( $0 < r/g < 1$ ). Further behind the crack tip ( $r/g > 1$ ), mode II displacements exhibit an oscillatory decay about zero with extreme values corresponding to changes in crack direction, *i.e.*, peaks and valleys of the sawtooth. The results for  $\alpha = 30^\circ$  and  $\alpha = 45^\circ$  are similar in character, but the  $\alpha = 45^\circ$  results show a greater mode II displacement amplitude. The mode I displacements ( $v^*$ ) also match the analytical solutions, but far from the crack tip the numerical solutions approach those expected of a straight crack. The finite element results in Figure 7 suggest mode II elastic displacements are greatest at the asperity nearest the crack tip, but mode I

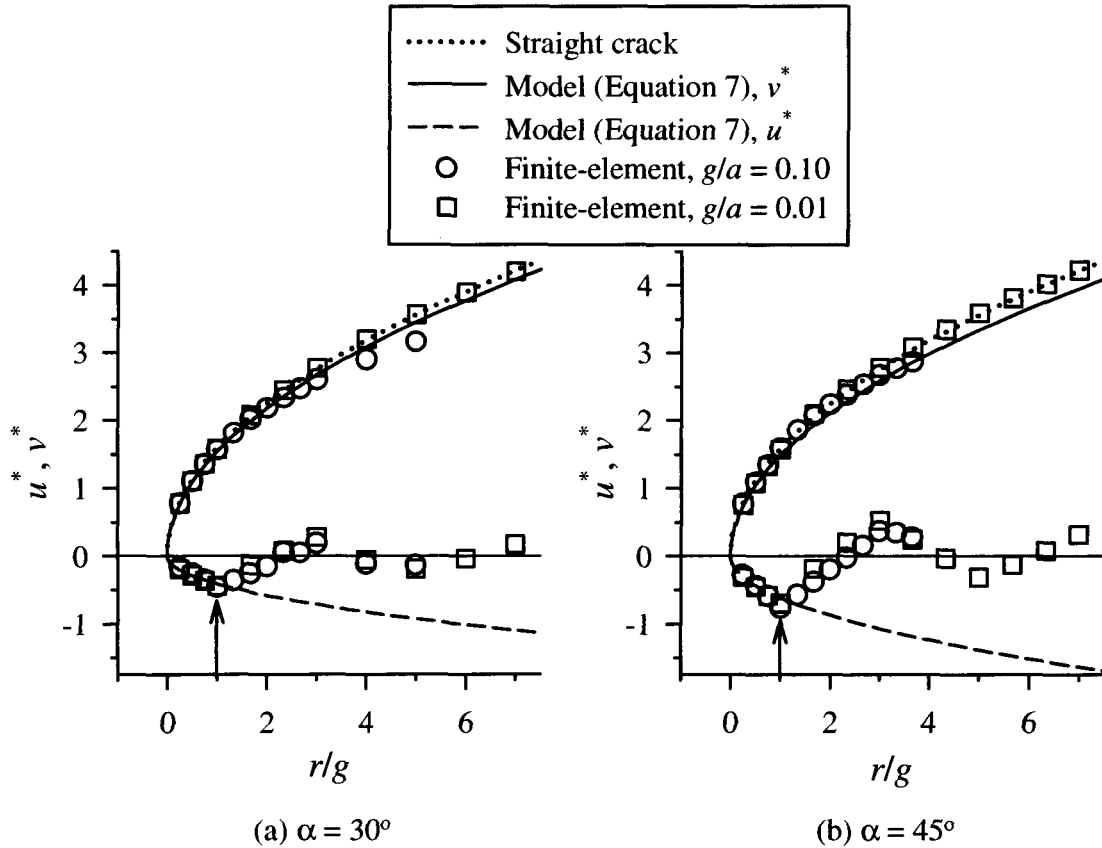


Figure 7. Elastic crack-face displacements of sawtooth cracks (under mode I loading) from finite-element analyses and analytical model solutions.

displacements are smaller here than at any other asperity in the crack wake. Consequently, RICC is most likely to occur at the asperity nearest the crack tip. Where crack roughness effects are important only this first asperity needs to be considered; asperities further behind the crack tip can be neglected. This observation is consistent with finite difference results of Llorca, who reported mode II displacements were greater at asperity peaks and valleys than intermediate points (ref. 13). However, Llorca did not indicate that the asperity nearest the crack tip was the location where RICC was most likely.

## Evaluation of Closure Levels

For rough cracks under applied mode I loading, finite element results reveal that crack-face contact might first occur at the asperity nearest the crack-tip. However, initial contact is expected at the crack tip for flat cracks (no roughness) because the elastic displacements are zero (ref. 49). In general, crack closure can first occur either at the crack tip (called tip contact) or at the asperity nearest the crack tip (called asperity contact). Simple geometric relationships are established here to determine crack closure levels for both types of crack face contact. A schematic of a sawtooth crack with an oxide layer is shown in Figure 8, where small boxes enclose the crack-tip and first asperity (a distance  $g$  behind the crack tip). Open arrows indicate high magnification schematics of these locations at the bottom of the figure. For asperity contact (left side of figure) the total opening and sliding displacements are labeled as  $(2v + \text{CTOD})$  and  $(2u + \text{CTSD})$ , respectively, and oxide layer thickness is indicated ( $t$ ) as the shaded region. For convenience, local coordinates are used to describe asperity contact. For tip contact (right side of figure), only plastic displacements occur at the crack tip, so only  $\text{CTOD}'$  and  $t$  are labeled in the lower right corner of Figure 8. Crack-tip coordinates are used to describe tip contact. The geometric relations satisfied for asperity contact and tip contact are shown in Equations 21 and 22, respectively. The  $\xi$  terms in these equations account for residual crack wake plasticity. In Equation 21, the absolute value of the mode II quantity  $(2u_{cl} + \text{CTSD})$  is used because sliding mode displacements in either direction promotes closure. Quantities with the subscript 'cl' correspond to values evaluated at crack face contact. Because elastic displacements are proportional to  $K$  and plastic displacements depend on  $(K_{\max})^2$  and  $(\Delta K)^2$ , all

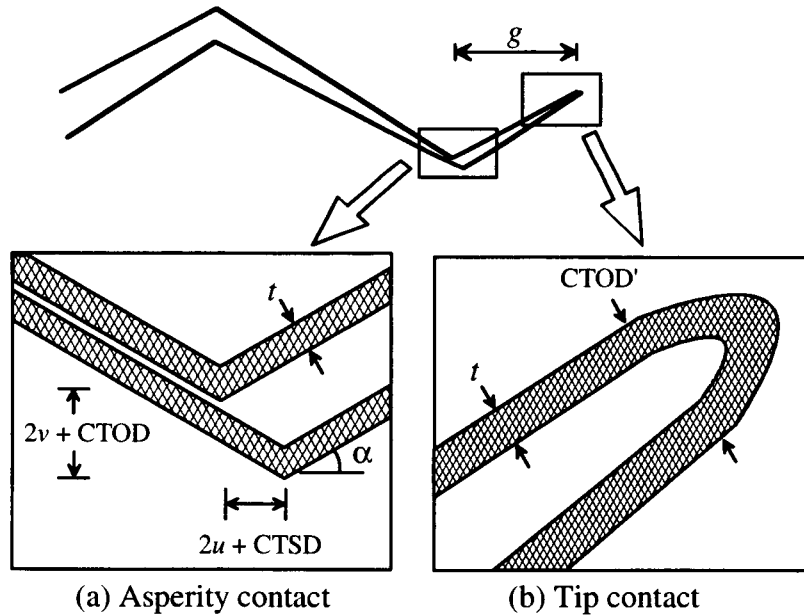


Figure 8. A schematic of a rough sawtooth crack (top of figure) to highlight the two locations where closure may first occur; at the asperity nearest the crack tip or at the crack tip.

displacements can be expressed in terms of load ratio at closure ( $R_{cl}$ ), as in Equations 23 and 24. Combining Equations 21-24 allows the closure level,  $R_{cl} = K_{cl} / K_{max}$ , to be determined at both critical locations.<sup>\*\*\*</sup> Contact at either location will affect the crack-tip driving force. Therefore, the greater of the two closure levels calculated from Equations 21 and 22 is used as the  $R_{cl}$  affecting crack-tip behavior.

$$(2v_{cl} + CTOD_{cl})\cos(\alpha) - |(2u_{cl} + CTSD_{cl})\sin(\alpha)| = 2t + \zeta \frac{CTOD_{max}}{\cos(\alpha)} \quad (21)$$

$$CTOD_{cl} = 2t + \zeta(CTOD_{max})' \quad (22)$$

$$\begin{Bmatrix} u_{cl} \\ v_{cl} \end{Bmatrix} = R_{cl} \begin{Bmatrix} u_{max} \\ v_{max} \end{Bmatrix} \quad (23)$$

$$\begin{Bmatrix} CTOD_{cl} \\ CTSD_{cl} \end{Bmatrix} = \left( \frac{3}{4} + \frac{1}{2} R_{cl} - \frac{1}{4} R_{cl}^2 \right) \begin{Bmatrix} CTOD_{max} \\ CTSD_{max} \end{Bmatrix} \quad (24)$$

## Summary

A fatigue crack closure model (called the CROP model) has been developed that includes plasticity-, roughness-, and oxide-induced crack closure mechanisms (PICC, RICC, and OICC, respectively). The CROP model is uniquely suited for a wide range of  $\Delta K$ , including threshold, because it accounts for the three closure mechanisms most likely at FCG threshold. Finite-element results indicate that RICC is most likely to occur first at the asperity nearest the crack tip because mode II displacements are greater and mode I displacements are less than at any other crack-wake asperity. However, PICC models indicate closure first occurs at the crack tip where crack roughness is not a factor. The CROP model considers both the crack tip, and the asperity nearest the crack tip, as potential locations where closure first occurs (called tip contact and asperity contact, respectively). Non-linear interactions between PICC, RICC, and OICC predicted by the CROP model are verified with experimental data in reference 22.

## References

1. W. Elber, "Fatigue Crack Closure Under Cyclic Tension," *Engineering Fracture Mechanics*, Volume 2, 1970, pp. 37-45.
2. N. J. Adams, "Fatigue Crack Closure at Positive Stresses," *Engineering Fracture Mechanics*, Volume 4, 1972, pp. 543-554.
3. S. Purshothaman and J. K. Tien, "A Fatigue Crack Growth Mechanism for Ductile Materials," *Scripta Metallurgica*, Volume 9, 1975, pp. 923-926.
4. N. Walker and C. J. Beevers, "A Fatigue Crack Closure Mechanism in Titanium," *Fatigue of Engineering Materials and Structures*, Volume 1, 1979, pp. 135-148.
5. K. Endo, K. Komai, and Y. Matasuda, "Mechanical Effects of Corrosion Products in Corrosion Fatigue Crack Growth of a Steel," *Bulletin of the JSME*, Volume 24, 1981, pp. 1319-1325.

---

<sup>\*\*\*</sup> Crack closure is quantified in terms of the load ratio where closure occurs,  $R_{cl}$ , (called closure level).

6. S. Suresh, G. F. Zaminski, and R. O. Ritchie, "Oxide Induced Crack Closure: An Explanation for Near-Threshold Corrosion Fatigue Crack Growth Behavior," *Metallurgical Transactions*, Volume 12A, 1981, pp. 1435-1443.
7. J. C. Newman, Jr. and W. Elber, "Summary," *Mechanics of Fatigue Crack Closure*, ASTM STP 982, J. C. Newman, Jr. and W. Elber, Editors, American Society for Testing and Materials, 1988, Philadelphia, PA, pp. 637-644.
8. R. O. Ritchie and S. Suresh, "Some Considerations on Fatigue Crack Closure at Near Threshold Stress Intensities Due to Fracture Surface Morphology," *Metallurgical Transactions*, Volume 13A, 1982, pp. 937-940.
9. J. C. Newman, Jr., "Analyses of Fatigue Crack growth and Closure Near Threshold Conditions for Long-Crack Behavior," *Fatigue Crack Growth Thresholds, Endurance Limits, and Design*, ASTM STP 1372, J. C. Newman, Jr. and R. S. Piascik, Editors, American Society for Testing and Materials, 2000, West Conshohocken, PA, pp. 227-251.
10. K. T. Venkateswara Rao and R. O. Ritchie, "Fatigue of Aluminum-Lithium Alloys," *International Material Reviews*, Volume 37, 1992, pp. 153-185.
11. S. Suresh and R. O. Ritchie, "A Geometric Model for Fatigue Crack Closure Induced by Fracture Surface Roughness," *Metallurgical Transaction*, Volume 13A, 1982, pp. 1627-1631.
12. S. H. Wang, C. Muller, and H. E. Exner, "A Model for Roughness-Induced Fatigue Crack Closure," *Metallurgical and Materials Transactions*, Volume 29A, 1998, pp. 1933-1939.
13. J. Llorca, "Roughness Induced Fatigue Crack Closure: A Numerical Study," *Fatigue and Fracture of Engineering Materials and Structures*, Volume 15, 1992, pp. 665-669.
14. A. M. Garcia and H. Seheitoglu, "Contact of Crack Surfaces During Fatigue: Part 1 – Formulation of the Model," *Metallurgical Transactions*, Volume 28A, 1997, pp. 2263-2275.
15. H. Seheitoglu and A. M. Garcia, "Contact of Crack Surfaces During Fatigue: Part 2 – Simulations," *Metallurgical Transactions*, Volume 28A, 1997, pp. 2277-2289.
16. N. Chen and F. V. Lawrence, "An Analytical Model for Studying Roughness Induced Crack Closure," *Fatigue and Fracture Mechanics, 29<sup>th</sup> Volume*, ASTM STP 1321, T. L. Panontin and S. D. Sheppard, Editors, American Society for Testing and Materials, 1999, West Conshohocken, PA, pp. 535-550.
17. K. S. Ravichandran, "A Theoretical Model for Roughness Induced Crack Closure," *International Journal of Fracture*, Volume 44, 1990, pp. 97-110.
18. K. S. Ravichandran, "Further Results on 'A Theoretical Model for Roughness Induced Crack Closure'; Effect of Yield Strength and Grain Size," *International Journal of Fracture*, Volume 44, 1990, pp. R23-R26.
19. J. C. Newman, Jr., "A Crack-Closure Model for Predicting Fatigue Crack Growth Under Aircraft Spectrum Loading," *Methods and Models for Predicting Fatigue Crack Growth Under Random Loading*, ASTM STP 748, J. B. Chang and C. M. Hudson, Editors, American Society for Testing and Materials, 1981, Philadelphia, PA, pp. 53-84.
20. F. Erdogan and G. C. Sih, "On the Crack Extension in Plates Under Plane Loading and Transverse Shear," *Journal of Basic Engineering*, December 1963, pp. 519-527.
21. K. Tanaka, Y. Akiniwa, Y. Nakai, and R. P. Wei, "Modeling of Small Fatigue Crack Growth Interacting with Grain Boundary," *Engineering Fracture Mechanics*, Volume 24, 1986, pp. 803-819.



22. J. A. Newman, W. T. Riddell, and R. S. Piascik, "Analytical and Experimental Study of Near-Threshold Interactions Between Crack Closure Mechanisms," 2003, NASA-TM-2003-211755.
23. J. A. Newman, *The Effects of Load Ratio on Threshold Fatigue Crack Growth of Aluminum Alloys*, Ph.D. dissertation, 2000, Virginia Polytechnic Institute and State University.
24. ASTM Standard E647, *Standard Test Method for Measurement of Fatigue Crack Growth Rates*, Annual Book of ASTM standards, Volume 3.01, American Society for Testing and Materials, 2001, West Conshohocken, PA.
25. G. C. Sih, *Handbook of Stress-Intensity Factors*, Institute of Fracture and Solid Mechanics, Lehigh University, 1973, Bethlehem, PA, pp. 1.2.1-1 and 1.2.1-2.
26. H. Tada, P. Paris, and G. Irwin, *The Stress Analysis of Cracks Handbook*, Del Research Corporation, 1985, Saint Louis, MO.
27. Y. Z. Chen, "Stress Intensity Factors for Curved and Kinked Cracks in Plane Extension," *Theoretical and Applied Fracture Mechanics*, Volume 31, 1999, pp. 223-232.
28. N. E. Dowling, *Mechanical Behavior of Materials*, p. 317, Prentice Hall, 1993, Englewood Cliffs, NJ.
29. G. R. Irwin, "Analysis of Stresses and Strains Near the End of a Crack Traversing a Plate," *Journal of Applied Mechanics*, Volume 24, 1957, pp. 361-364.
30. D. S. Dugdale, "Yielding of Steel Sheets Containing Slits," *Journal of the Mechanics and Physics of Solids*, Volume 8, 1960, pp. 100-104.
31. A. J. Wilkinson and S. G. Roberts, "A Dislocation Model for the Two Critical Stress Intensities Required for Threshold Fatigue Crack Propagation," *Scripta Materialia*, Volume 35, 1996, pp. 1365-1371.
32. B. A. Bilby, A. H. Cottrell, and K. H. Swinden, "The Spread of Plastic Yield from a Notch," *Proceedings of the Royal Society*, Volume A272, 1963, pp. 304-314.
33. J. Weertman, *Dislocation Based Fracture Mechanics*, World Scientific Publishing Company, 1996, River Edge, NJ.
34. J. Dundurs and T. Mura, "Interaction Between an Edge Dislocation and a Circular Inclusion," *Journal of the Mechanics and Physics of Solids*, Volume 12, 1964, pp. 177-189.
35. R. Pippan, "The Condition for the Cyclic Plastic Deformation of the Crack Tip: The Influence of Dislocation Obstacles," *International Journal of Fracture*, Volume 58, 1992, pp. 305-318.
36. H. W. Liu, "A Dislocation Barrier Model for Fatigue Limit – As Determined by Crack Non-Initiation and Crack Non-Propagation," *International Journal of Fracture*, Volume 96, 1999, pp. 331-344.
37. B. A. Bilby, A. H. Cottrell, and K. H. Swinden, "The Spread of Plastic Yield from a Notch," *Proceedings of the Royal Society*, Volume A272, 1963, pp. 304-314.
38. R. E. Reed-Hill, *Physical Metallurgy Principles*, 2<sup>nd</sup> Edition, PWS Publishers, 1973, Boston, MA, pp. 171-173.
39. H. Gao, N. Alagok, M. W. Brown, and K. J. Miller, "Growth of Fatigue Cracks Under Combined Mode I and Mode II Loads," *Multiaxial Fatigue, ASTM STP 853*, K. J. Miller and M. W. Brown, Editors, American Society for Testing and Materials, 1985, Philadelphia, PA, pp. 184-202.

40. J. D. Eshelby, F. C. Frank, and F. R. N. Nabarro, "The Equilibrium of Linear Arrays of Dislocations," *Philosophical Magazine*, Volume 42, 1951, pp. 351-364.
41. P. K. Liaw, "Overview of Crack Closure at Near-Threshold Fatigue Crack Growth Levels," *Mechanics of Fatigue Crack Closure*, ASTM STP 982, J. C. Newman, Jr. and W. Elber, Editors, American Society for Testing and Materials, 1988, Philadelphia, PA, pp. 62-92.
42. B. Budiansky and J. W. Hutchinson, "Analysis of Closure in Fatigue Crack Growth," *Journal of Applied Mechanics*, Volume 45, 1978, pp. 267-276.
43. S. Suresh, A. K. Vasudevan, and P. E. Bretz, "Mechanisms of Slow Fatigue Crack Growth in High Strength Aluminum Alloys: Role of Microstructure and Environment," *Metallurgical Transactions*, Volume 15A, 1984, pp. 369-379.
44. M. S. Hunter and P. Fowle, "Natural and Thermally Formed Oxide Films on Aluminum," *Journal of the Electrochemical Society*, Volume 103, 1956, pp. 482-485.
45. S. Suresh and R. O. Ritchie, "Some Consideration on the Modeling of Oxide-Induced Fatigue Crack Closure using Solutions for a Rigid Wedge inside a Linear Elastic Crack," *Scripta Metallurgical*, Volume 17, 1983, pp. 575-580.
46. J. A. Ruppen and R. Salzbrenner, "The Effect of Environment on Crack Closure and Fatigue Threshold," *Fatigue of Engineering Materials and Structures*, Volume 6, 1983, pp. 307-314.
47. P. A. Wawrzynek and A. R. Ingraffea, "FRANC2D: A Two-Dimensional Crack Propagation Simulator," 1994, NASA CR-4572.
48. I. S. Raju and K. N. Shivakumar, "An Equivalent Domain Integral Method in the Two-Dimensional Analysis of Mixed Mode Crack Problems," *Engineering Fracture Mechanics*, Volume 37, 1990, pp. 707-725.
49. W. T. Riddell and R. S. Piascik, "Stress Ratio Effects on Crack Opening Loads and Crack Growth Rates in Aluminum Alloy 2024," 1998, NASA-TM-1998-206929.

REPORT DOCUMENTATION PAGE			Form Approved OMB No. 0704-0188	
Public reporting burden for this collection of information is estimated to average 1 hour per response, including the time for reviewing instructions, searching existing data sources, gathering and maintaining the data needed, and completing and reviewing the collection of information. Send comments regarding this burden estimate or any other aspect of this collection of information, including suggestions for reducing this burden, to Washington Headquarters Services, Directorate for Information Operations and Reports, 1215 Jefferson Davis Highway, Suite 1204, Arlington, VA 22202-4302, and to the Office of Management and Budget, Paperwork Reduction Project (0704-0188), Washington, DC 20503.				
1. AGENCY USE ONLY (Leave blank)		2. REPORT DATE May 2003		3. REPORT TYPE AND DATES COVERED Technical Memorandum
4. TITLE AND SUBTITLE Modeling the Interactions Between Multiple Crack Closure Mechanisms at Threshold			5. FUNDING NUMBERS  706-62-31-51	
6. AUTHOR(S) John A. Newman, William T. Riddell, and Robert S. Piascik				
7. PERFORMING ORGANIZATION NAME(S) AND ADDRESS(ES) NASA Langley Research Center Hampton, VA 23681-2199 U.S. Army Research Laboratory Vehicle Technology Directorate NASA Langley Research Center Hampton, VA 23681-2199			8. PERFORMING ORGANIZATION REPORT NUMBER  L-18279	
9. SPONSORING/MONITORING AGENCY NAME(S) AND ADDRESS(ES) National Aeronautics and Space Administration Washington, DC 20546-0001 and U.S. Army Research Laboratory Adelphi, MD 20783-1145			10. SPONSORING/MONITORING AGENCY REPORT NUMBER  NASA/TM-2003-212402 ARL-TR-2959	
11. SUPPLEMENTARY NOTES				
12a. DISTRIBUTION/AVAILABILITY STATEMENT Unclassified-Unlimited Subject Category 26 Availability: NASA CASI (301) 621-0390 Distribution: Standard			12b. DISTRIBUTION CODE	
13. ABSTRACT (Maximum 200 words) A fatigue crack closure model is developed that includes interactions between the three closure mechanisms most likely to occur at threshold; plasticity, roughness, and oxide. This model, herein referred to as the CROP model (for Closure, Roughness, Oxide, and Plasticity), also includes the effects of out-of-plane cracking and multi-axial loading. These features make the CROP closure model uniquely suited for, but not limited to, threshold applications. Rough cracks are idealized here as two-dimensional sawtooths, whose geometry induces mixed-mode crack-tip stresses. Continuum mechanics and crack-tip dislocation concepts are combined to relate crack face displacements to crack-tip loads. Geometric criteria are used to determine closure loads from crack-face displacements. Finite element results, used to verify model predictions, provide critical information about the locations where crack closure occurs.				
14. SUBJECT TERMS Fatigue crack growth, Crack closure, Plasticity, Roughness, Oxide, Crack tip, Experiment, Threshold			15. NUMBER OF PAGES 22	
			16. PRICE CODE	
17. SECURITY CLASSIFICATION OF REPORT Unclassified	18. SECURITY CLASSIFICATION OF THIS PAGE Unclassified	19. SECURITY CLASSIFICATION OF ABSTRACT Unclassified	20. LIMITATION OF ABSTRACT UL	